ANL/ET/CP-98708

STRESS CORROSION CRACKING OF AUSTENITIC STAINLESS STEEL CORE INTERNAL WELDS*

H. M. Chung, J.-H. Park, W. E. Ruther, J. E. Sanecki, R. V. Strain, and N. J. Zaluzec
Argonne National Laboratory
Argonne, IL 60439, USA

March 1999

To be presented at Corrosion '99, April 25-30, 1999, San Antonio, Texas.

*Work supported by the U.S. Nuclear Regulatory Commission, Office of Nuclear Regulatory Research.

DISCLAIMER

DISCLAIMER

Portions of this document may be illegible in electronic image products. Images are produced from the best available original document.

STRESS CORROSION CRACKING OF AUSTENITIC STAINLESS STEEL CORE INTERNAL WELDS

H. M. Chung, J.-H. Park, W. E. Ruther, J. E. Sanecki, R. V. Strain, and N. J. Zaluzec
Argonne National Laboratory
9700 South Cass Avenue
Argonne, IL 60439

ABSTRACT

Microstructural analyses by several advanced metallographic techniques were conducted on austenitic stainless steel mockup and core shroud welds that had cracked in boiling water reactors. Contrary to previous beliefs, heat-affected zones of the cracked Type 304L, as well as 304 SS core shroud welds and mockup shielded-metal-arc welds, were free of grain-boundary carbides, which shows that core shroud failure cannot be explained by classical intergranular stress corrosion cracking. Neither martensite nor delta-ferrite films were present on the grain boundaries. However, as a result of exposure to welding fumes, the heat-affected zones of the core shroud welds were significantly contaminated by oxygen and fluorine, which migrate to grain boundaries. Significant oxygen contamination seems to promote fluorine contamination and suppress thermal sensitization. Results of slow-strain-rate tensile tests also indicate that fluorine exacerbates the susceptibility of irradiated steels to intergranular stress corrosion cracking. These observations, combined with previous reports on the strong influence of weld flux, indicate that oxygen and fluorine contamination and fluorine-catalyzed stress corrosion play a major role in cracking of core shroud welds.

Key words: core shroud weld, intergranular stress corrosion cracking, weld flux, oxygen and fluorine contamination, grain-boundary Cr depletion

INTRODUCTION

Failure of welded core internal components such as core shrouds, usually fabricated from Type 304 and 304L austenitic stainless steels (SSs), has increased significantly in boiling water reactors (BWRs). Although BWR core shrouds are subject to relatively low neutron fluence, many vertical and horizontal welds crack by the time they accumulate relatively low fluences of $\approx 3 \times 10^{20}$ n cm^{-2}. At these low fluences, nonwelded base-metal components would not be considered susceptible to irradiation-assisted stress corrosion cracking (IASCC), which typically occurs after a threshold fluence of $\approx 5 \times 10^{20}$ n cm^{-2}. Because of this, and in view of the understanding gained from stress corrosion cracking of gas-tungsten-arc-welded (GTA-welded) piping and laboratory-sensitized nonwelded base-metal specimens, most cases of core shroud cracking have been attributed to classical intergranular stress corrosion cracking (IGSCC) of thermally sensitized SS, in which significant grain-boundary carbide precipitation occurs in the heat-affected zone (HAZ) during welding or sensitizing heat treatment. However, an increasing number of cracking incidents observed in core shrouds fabricated from Type

304L SS are difficult to explain on the basis of classical IGSCC, because grain-boundary carbide precipitation would not be expected to occur in low-C SSs. Some investigators hence have suspected that grain-boundary Cr depletion could occur in Type 304L SS core shroud welds via an irradiation-induced process even if the total accumulated fluence is low. In contrast to pipings and small components that are welded by GTA procedure in an inert atmosphere, large core internals such as BWR core shrouds are welded in air by a shielded-metal-arc (SMA) or submerged-arc (SA) procedure, in which weld electrodes coated with F-containing flux are used to produce a plasma shield around the arc-melted plates. For such circumstances, it was suggested that the deleterious effects of O[1,2] and F[2,3] contamination could be significant. In this study, to provide a better understanding of the core shroud cracking mechanism, microchemical and microstructural characteristics of unirradiated mockup welds and field-cracked Type 304 and 304L SS core shroud welds were investigated systematically by chemical analysis, scanning electron microscopy (SEM), Auger electron spectroscopy (AES), secondary-ion mass spectroscopy (SIMS), and field-emission-gun advanced analytical electron microscopy (FEG AAEM). Slow-strain-rate tensile (SSRT) tests were also conducted to determine the effect of F contamination on the susceptibility of irradiated steels to stress corrosion cracking.

MATERIALS AND EXPERIMENTAL PROCEDURES

Chemical compositions and types of the stainless steels used to produce mockup SMA and GTA welds are given in Table 1. Also in Table 2 are steel types, fast neutron fluences, and chemical compositions of the BWR core shrouds investigated in this study. Details of stress corrosion testing and microstructural analysis in a JEOL JAMP-10 automated scanning Auger microscope (SAM) are available elsewhere.[2,3] Microstructural analysis by transmission electron microscopy (TEM) was conducted in either a Vacuum Generator HB-603 FEG AAEM or a JEOL 100CX-II scanning transmission electron microscope (STEM). Ion mapping by Cameca 4F SIMS was conducted by using Cs^+ ion as the sputtering and primary beam at 10 kV and 150 nA. Slow-strain-rate tensile (SSRT) tests were conducted in simulated BWR water at 289°C at a fixed strain rate of 1.65×10^{-7} s^{-1} (see Ref. 2).

MOCKUP CORE SHROUD WELDING

To simulate the microstructure of a core shroud horizontal weld, mockup SMA welds were prepared from the steel plates described in Table 1. For comparison, GTA welds were also prepared from the same plates. The SMA procedure, which is shown schematically in Fig. 1, uses welding electrodes that are coated with a welding flux. In SA welding, a similar flux is used in powder form to cover the base-metal plate. Consequently, similar impurity contamination occurs in the weld and heat-affected zones (WZ and HAZ) in both types of welds. Vertical welds in a core shroud are usually welded by an SA procedure, whereas horizontal welds are prepared by an SMA procedure. Composition of the SMA welding electrodes, described in ASME Specification Section II SFA 5.4, "Specification for Stainless Steel Electrodes for Shielded Metal Arc Welding," is given in Table 3. The electrode consists of ≈60% coating and ≈40% Type 308 SS. Fluorine was contained in granules of fluorspar dispersed in the silicate binder. Fluorine content in the electrode coating, determined by separate chemical analysis, was ≈2.86 wt.%, and analysis by SEM energy-dispersive spectroscopy confirmed the presence of CaF_2.[3] Fluorspar is readily vaporized during welding and produces a plasma shield over the molten steel under the high voltage applied.

The SMA and GTA welds from the 12.7-mm-thick plates described in Table 1 were prepared by making 8 and 18 weld passes, respectively. However, SMA welds of the 38-mm-

thick plates required as many as 38 weld passes. A schematic diagram of the welding passes and TEM disk locations of the 38-mm-thick plate of Type 304 SS, Heat 19611, is shown in Fig. 2. Weld slag and slag pockets were removed after each welding pass. Weld slags trapped in the weld cusps were removed with a grinding wheel.

STRUCTURE AND PROPERTIES OF MOCKUP CORE SHROUD WELDS

Chemical Analysis. Compositions of the SMA and GTA weld HAZs of Type 304 SS Heat C1, determined by wet chemistry, are summarized in Table 4. Oxygen and Mo contents of the SMA and GTA (or tungsten inert gas, TIG) weld HAZs of the Type 304 SS Heat C1, Type 304L SS Heat C3, and Type 316 SS Heat C21 are plotted in Fig. 3. Oxygen and Mo contents of the base metals of the heats are also shown in the figure for comparison. While contamination in the GTA weld HAZ was insignificant, the SMA weld HAZ was significantly contaminated by O, Mo, and F, the elements from the E-308-16 electrode or air.

Analysis by SIMS. Distributions of O, F, and other impurities were analyzed by SIMS on the SMA and GTA welds of a Type 304 SS, Heat C1 and the SMA weld of the Type 304L SS, Heat C3. Results of mapping in color of the secondary ions of O, F, Ca, C, and N from the weld zone and HAZ were obtained using Cs^+ as primary ion (see Fig. 4). Black, red, orange, and white in the map correspond, respectively, to regions of proportionately higher ion population; black corresponds to no or negligible ions detected, and white corresponds to the highest ion population. For the ion maps given in the figure, the boundaries between WZ and HAZ are also marked. The results of the SIMS analyses can be summarized as follows:

(a) Oxygen and F contamination was significant in all SMA welds. Oxygen contamination was significantly more pronounced in the WZ than in the HAZ.

(b) In contrast to SMA welds, F contamination was negligible and O contamination was less significant in GTA welds.

(c) Sparsely populated oxide inclusions were present in the base metal of Type 304 SS Heat C1. These oxides were rich in F, showing that the base metal of this heat of Type 304 SS contained F in spherical oxide inclusions that formed during the ingot-melting process.

(d) Nitrogen and C contamination was insignificant in the SMA, as well as in GTA welds.

(e) Significant carbide precipitation occurred in the HAZ of the GTA weld. In contrast to oxides, F atoms were not enriched in the carbides, which is consistent with the results of AES analyses of BWR neutron-absorber tubes reported previously.[2]

(f) Carbide precipitation was negligible in the HAZ of the SMA weld of Type 304 SS Heat C1 (≈0.060 wt.% C), as well as in Type 304L SS Heat C3 (≈0.016 wt.% C). That is, in contrast to GTA welding, thermal sensitization did not occur during SMA welding, even in high-C Heat C1.

(g) Calcium-rich precipitates were present in SMA welds in the WZ and in the HAZ up to ≈0.6 mm away from the fusion line. Most of the precipitates were also rich in O and F. No calcium-rich precipitates were present in GTA welds.

Because calcium-rich precipitates were absent in GTA welds, they are not likely to be (Ca,Mn)S-type sulfides, which are observed in some steels;[2] they are more likely to have been produced in association with the SMA welding procedures. To confirm this, chemical

compositions of the calcium-rich precipitates were determined in an SEM by energy-dispersive spectroscopy. The results are shown in Fig. 5. The calcium-rich precipitates were high in O, F, and Si, the same elements that are also high in the flux compound in the weld electrode coating (Table 3). The composition of the surface weld slag was similar but contained more Si, K, and Ti. Therefore, it is obvious that the calcium-oxyfluoride-type precipitates form in association with the contamination that occurs during the SMA welding. After each welding pass, the weld slag pockets were removed mechanically from weld cusps by a grinding wheel, and this process may have assisted the formation of the Ca-rich precipitates by impregnating small particles of broken weld scale. The Ca-rich inclusions dissolved readily when in contact with water during either SSRT testing at 288°C or polishing at room temperature. When the specimen surface was polished in an oxalic solution, however, the inclusions did not dissolve. These observations indicate that the calcium-oxyfluoride-type inclusions are soluble in reactor coolants and hence could accelerate the release of F ions into the crack tip.

Analysis by TEM. The absence of carbide precipitates in the SIMS maps of the HAZ of the SMA weld of high-C Type 304 SS, Heat C1 (≈0.060 wt.% C) was a major surprise, because in contrast to a GTA weld, this means that an SMA weld of Type 304 SS would not exhibit thermal sensitization via grain-boundary carbide precipitation. Therefore, extensive characterization of grain-boundary carbide precipitation was conducted by TEM to investigate more directly the relative behavior of thermal sensitization in the GTA and SMA welds. Disks for TEM analysis were punched from the HAZ and base metal, as illustrated in Fig. 2. Grain-boundary carbides were characterized by the usual combination of bright-field imaging, tilting, selected-area-diffraction (SAD) analysis, and dark-field imaging. As expected, many $M_{23}C_6$ carbides, 70-150 nm in size, were observed on the grain boundaries of HAZ of the GTA welds. This is shown in Fig. 6, which includes a dark-field image of grain-boundary carbides and a characteristic diffraction pattern that contains many weak reflections originating from the grain-boundary $M_{23}C_6$.

In contrast, carbides were absent on grain boundaries of the HAZ of the mockup SMA welds, regardless of the location of the thin-foil TEM specimens relative to the free surface or weld fusion line. A typical example of grain boundaries in the HAZ of the SMA weld of high-carbon (≈0.06 wt.%) Type 304 SS, Heat C1, is shown in Fig. 7. Carbides were also absent on grain boundaries of the HAZs of the SMA welds of the Type 316 SS, Heat C21 (≈0.060 wt.% C) and the low-carbon (≈0.016 wt.%) Type 304L SS, Heat C3. Consistent with the observation made on the 12.7-mm-thick SMA welds, no grain-boundary carbides were detected in any of the TEM disks from the HAZs of the 38-mm-thick SMA welds of the Type 304 SS, Heat 19611 or Heat M9284. An example of "clean" (i.e., carbide-free) grain boundaries typical of the HAZ of the SMA weld of Heat 19611 is also shown in Fig. 7. Neither bright-field images nor diffraction spots from $M_{23}C_6$ precipitates, characteristic of a sensitized GTA weld HAZ, were present on more than 25 grain boundaries examined, and hence no dark-field images could be obtained. This shows that grain-boundary carbide precipitation was absent in the SMA weld of this heat. Dark-field imaging accompanied by SAD indexing is conclusive evidence of grain-boundary carbide precipitation. In contrast to the SMA weld of Type 304 SS, Heat M9284, grain-boundary carbides were conclusively identified in the HAZ of the 38-mm-thick GTA weld of the same heat. This is consistent with the observations made on the 12.7-mm-thick GTA welds of Type 304 SS, Heat C1 and Type 316 SS, Heat C21.

Results of the TEM characterization of thermal sensitization via grain-boundary carbide precipitation in the nonirradiated SMA and GTA welds are summarized in Table 5. For Type 304 and 316 SS heats listed in the table, grain-boundary carbides were observed in the HAZs of all GTA welds, whereas grain-boundary carbides were not observed in the HAZs of any of

the SMA welds. This shows that susceptibility to thermal sensitization is negligible in SMA welds, which is in major contrast to the behavior of GTA welds. It is possible that high O contamination associated with SMA welding suppresses grain-boundary carbide precipitation because the affinity of Cr to O atoms is stronger than the affinity of Cr to C atoms.

STRUCTURE AND PROPERTIES OF TYPE 304 SS BWR-D CORE SHROUD WELD

A Type 304 SS core shroud sample that accumulated a fluence of ≈1 x 10^{20} n·cm^{-2} (E >1 MeV) and had cracked during service in BWR-D was obtained for microstructural analysis by TEM and AES. The boat sample was sectioned from the cracked core plate support ring. Cracks in the Type 304 SS (≈0.063 wt.%C) ring were detected near the horizontal H5 weld along the entire circumference (see Fig. 8). In many later-design BWRs, the H5 weld is referred to as the H6A weld. The low-magnification optical photomicrograph in Fig. 9 shows three cracks in the boat sample; a high-magnification photomicrograph is shown in Fig. 10. Cold-worked grains are visible in the HAZ near the #1 crack, which nucleated ≈3.5 mm away from the fusion line. The other two cracks are located ≈9 and ≈14 mm away from the fusion line, apparently in the base metal. Compared to the surface region (Fig. 10, top-left inset), the phenomena of grain encirclement and grain fallout were more pronounced in the crack tip regions (Fig. 10, top-right and bottom-left insets). Apparently, grain encirclement in the crack tip region occurred in the reactor during operation, and fallout of the encircled grains occurred at room temperature during mechanical polishing of the specimen. Grain encirclement could have been strongly influenced by the water chemistry in the crack tip crevice in which concentration of deleterious ions would be relatively higher, e.g., F ions dissolved gradually in the water from the surrounding grains in the contaminated HAZ.

Characterization by TEM of grain-boundary carbide precipitation and thermal sensitization was conducted on the boat sample shown in Fig. 9. A total of 16 TEM disks were prepared near the cracks located in the HAZ and base metal. Of the 16 disks, 8 were jet-polished and examined by TEM. No grain-boundary carbide was observed in any of the 8 disks that were examined. A typical example of carbide-free "clean" grain boundaries is shown in Fig. 11. Some disks exhibited a light-contrasted feature that is an indication of localized thinning during the jet-polishing procedure in association with significant inhomogeneity of local chemical composition. Because grain-boundary carbide precipitation was absent in the HAZ near the cracks, it is difficult to explain the cracking in the Type 304 SS shroud weld on the basis of classical thermal sensitization.

STRUCTURE AND PROPERTIES OF TYPE 304L SS BWR-C CORE SHROUD WELD

Microstructures of two boat samples from the field-cracked BWR-C core shroud weld, irradiated to a fluence of 4.6 x 10^{19} n·cm^{-2} (E >1 MeV), were characterized by SEM, FEG-AAEM, and AES. The fracture surface of the field crack was badly corroded because of exposure to the reactor coolant. However, regions of clean fracture surface morphology could be found near the tight crack tip. The fracture surface morphology (Fig. 12) is not a typical intergranular (IG) fracture but appears to contain a significant fraction of ductile tearing in addition to IG separation.

Neither carbide, Cr depletion, nor martensite thin film was detected on grain boundaries of HAZ specimens that were characterized by an HB603 FEG-AAEM (see Figs. 13 and 14). The Type 304L SS weld HAZ was not thermally sensitized, and grain-boundary Cr depletion by a thermal or irradiation-induced process was negligible. Therefore, cracking of this Type 304L core shroud weld cannot be explained on the basis of either classical IGSCC or IASCC.

Notched AES specimens were prepared from the core shroud weld HAZ and fractured at 23°C in the ultrahigh vacuum of the scanning Auger microscope. A typical example of the clean in-situ fracture surface morphology is shown in Fig. 15. The figure shows IG fracture surfaces and many fine particles (≈0.1-2 μm in size) on the grain boundaries. These particles were found to be either Cr oxides (see Fig. 16) or Fe-Ni spinel oxides. The area AES signal, acquired from a square region (≈10 x 10 μm) of an IG fracture surface, also showed an unusually high O peak, as well as weak signals of S, Mo, and F at 625 eV.[2] These observations indicate that O contamination in the core shroud HAZ was very significant

Similar evidence for presence of numerous grain-boundary oxide particles could be also obtained from AES analysis of polished specimens. An optical photomicrograph of a polished surface, obtained from the H3 weld HAZ of Type 304L SS BWR-C core shroud, is shown in Fig. 17. Besides elongated cold-worked grains, numerous inclusions are visible, many on or near grain boundaries. These inclusions located on or near grain boundaries are denoted with white arrows in the figure. To identify the inclusions, the polished specimen was analyzed by AES after sputtering a selected area with Ar ions for ≈300 s. On the surface of the sputtered specimen, many light-contrasted inclusions were visible in a secondary-electron image (Fig. 18). The light contrast indicates that the inclusions are insulators and are charged electrically. Most of the inclusions were found to be Fe- or spinel-type oxides (see Figs. 18). Some of the inclusions were identified as CaO, which is consistent with the observation of Ca oxyfluorides in the mockup core shroud weld by SIMS mapping (Fig. 4D). No carbides were observed. The presence of Fe oxides and CaO inclusions in both BWR-C core shroud and the mockup SMA weld HAZ is consistent with the premise that significant contamination by O and Ca occurred during welding. Furthermore, the high number density of oxides that were observed on the grain boundaries (Figs. 15 and 17) indicates that O atoms are concentrated on grain boundaries of the H3 weld HAZ of the BWR-C core shroud.

Many Fe oxides were also observed in the specimen prepared from HAZ of the H5 weld of the Type 304 SS BWR-D core shroud. As shown in the optical photomicrographs in Fig. 10, the number density of oxide inclusions was significantly lower in the Type 304 SS BWR-D shroud weld specimen than in the BWR-C specimen. This indicates that welding-related contamination was lower in the BWR-D H5 weld than in the BWR-C H3 weld.

The AES signals of F can be easily overlooked because the primary dN(E)/dE peak is hidden behind the strong Fe peak.[2] However, F gives rise to a weak secondary peak at ≈625 eV. Although results from AES analysis of F cannot be considered quantitative because of this limitation, results of an earlier analysis indicated that the relative F content of the weld is higher than the F content of the other components.[2,3] It was also reported that the F content in oxides and sulfides is relatively higher than that in the grain matrices of the base metals,[2] which is consistent with the results of SIMS ion mapping shown in Fig. 4. The greater concentrations of F on oxides appear to be consistent with the results of Shimizu et al.[4], who showed by SIMS that F is readily incorporated into tantalum oxides.

Solubilities of O and F in SSs are very low except at high temperatures. Therefore, to reduce the total free energy, O will either form oxides or segregate to grain boundaries in the HAZ during cooling from a high temperature close to the melting temperature of the steel. In the process, F seems to migrate to O-rich regions or oxide, or may even form an FO complex, as shown in the study of Shimizu et al.[4] It is also possible that O and F atoms segregate to grain boundaries during the long-term exposure to the reactor operating condition, i.e., at ≈289°C under neutron irradiation. Consistent with this prediction, a significant decrease in the intensity of F-625 eV signal was observed as function of sputtering distance from a grain-

boundary fracture surface that was produced in-situ and shown in Fig. 15. The decreasing intensity of F signal is shown in Fig. 19. The result of the figure indicates that F atoms have segregated to grain boundaries of the BWR-C core shroud weld HAZ.

SLOW-STRAIN-RATE TENSILE TESTING OF THE EFFECTS OF FLUORINE

The effect of F ions in water on IG stress corrosion cracking of nonirradiated sensitized SS was first reported by Ward et al.[5] Besides thermal sensitization, the following conditions were reported to exacerbate IG cracking in the base metal of Type 304 SS: (a) tensile stress, (b) cold work, (c) a crevice, or (d) visible oxide film. Similar effects for nonirradiated materials have been reported by other investigations on SS,[6-12] Inconel 182,[12] and brass.[13] Effects of F contamination on IGSCC of unirradiated flux-welded SSs have also been reported by several investigators,[5,8,9] the primary source of F being weld fumes, as in the present investigation.

In view of these reports, SSRT tests were conducted to determine more directly the effect of F contamination by immersing BWR neutron absorber tubes in a solution that contains HF. The high-purity absorber tubes irradiated to a fluence of 0.7×10^{21} n·cm^{-2} (E > 1 MeV) were immersed for 10 min in a solution of $10HF–15HNO_3–75H_2O$, followed by a 15 min rinse in distilled water and 3-4 h preconditioning in 289°C water before loading. The results, compared in Fig. 20 with those of the as–irradiated specimens, show significant effects on total strain and susceptibility to IGSCC. The specimens in Fig. 20 were covered with ≈20-μm-thick oxide layer that formed during service; thus, F from HF will be incorporated in the oxide and in the O-rich layer beneath the oxide. These brittle layers cracked readily with or without an immersion treatment; therefore, cracks appear to nucleate early during SSRT. Fluorine atoms, incorporated in the oxide and O-rich layer, appeared to slowly dissolve in the crack tip water and exacerbate IG crack propagation, which caused fracturing at a significantly lower plastic strain. The oxide layer on some specimens sloughed off, a phenomenon also reported by Ward et al.,[5] Bryant and Habicht,[8] and Takemoto et al.[9] This is shown in Fig. 21.

DISCUSSION

Microstructural characteristics of the cracked Type 304L and 304 SS core shrouds weld HAZ can be summarized by (a) absence of carbides on or near grain boundaries, (b) absence of martensite or delta-ferrite thin film on grain boundaries, (c) no or negligible grain-boundary Cr depletion, (d) dense dislocations, (e) significant O contamination and dense precipitation of tiny oxides on grain boundaries, (f) significant F contamination, and (g) evidence of O and F segregation to grain boundaries. Results obtained from the microstructural and microchemical analyses of the mockup nonirradiated SMA welds and the field-cracked core shrouds were essentially similar. Considering these observations, it is difficult to explain the core shroud weld cracking on the basis of either classical IGSCC, in which thermal sensitization by grain-boundary carbide precipitation plays the key role, or the grain-boundary Cr-depletion model of IASCC.

Fluorine-assisted intergranular SCC has been reported for unirradiated austenitic stainless steels by a number of investigators.[5-13] In most experiments, higher susceptibility to intergranular SCC was caused by fluoride ions that were added intentionally in the water.[5-13] However, in other experiments, the only source of F that produced higher susceptibility to intergranular SCC was the weld-fume contamination in flux-welded steels.[5,8,9] In the latter investigations, no microstructural characterization of grain-boundary carbides (e.g., by TEM) was conducted which may have provided a better understanding of the mechanism of fluorine-assisted acceleration of intergranular SCC. Although no direct evidence of grain-boundary

carbide precipitation was observed, it was assumed implicitly in these investigations that F contamination in flux-welded steels exacerbates susceptibility of HAZ to classical IGSCC (i.e., intergranular SCC driven by thermal precipitation of grain-boundary carbides and resultant grain-boundary Cr depletion).[5,8] Results of the direct microstructural characterization in the present investigation do not support this assumption. That is, the mechanism of intergranular SCC of weld-fume-contaminated HAZ of flux-welded steels, such as core shroud welds, appears to fundamentally differ from the mechanism of classical IGSCC.

The present investigation shows that significant F contamination of core shroud welds occurs in association with O contamination. The O and F contamination characteristics observed for the mockup SMA weld and the Type 304 and 304L BWR core shroud welds were essentially similar. The tandem contamination behavior of O and F explains well the previous reports by several investigators that welding fume contamination or the presence of surface oxide layer or weld slag strongly exacerbates the susceptibility of flux-welded steels to IGSCC.[5,8,9] The results from the present SSRT tests on the neutron absorber tubes are also consistent with the results of the bend-beam experiments of these investigators,[5,8] that is, F contamination in oxide-covered material is an important factor that exacerbates susceptibility to IG stress corrosion cracking.

Evidence was observed that O and F contents in the HAZ were higher on grain boundaries than in the base metal of core shroud welds. In consideration of this direct association of O and F contamination and segregation to grain boundaries, this type of intergranular SCC caused by material contamination by O and F in absence of grain-boundary carbide precipitation or Cr depletion, would be appropriately termed "oxyfluorine-assisted" SCC. In this type of SCC, a synergism among O, Cr, and F plays a primary role, and susceptibility to intergranular SCC is influenced strongly by the degree of O and F segregation to grain boundaries. This is because higher O on grain boundaries is conducive to more Cr bound to O and more F segregated to grain boundaries as a result of the fact that higher concentration of O increases significantly the local solubility of F atoms. This condition is conducive to higher F ion and lower Cr ion concentrations dissolved in the crack tip water, which allows a strong catalytic role of F on metal dissolution at the crack tip. The presence of Ca oxyfluoride precipitates appears to accelerate the process because the precipitates dissolve readily in water, thereby releasing F more rapidly in the crack tip water.

The following model is proposed to explain the mechanism of "oxyfluorine-assisted" SCC, which is based on a synergism among O, Cr, and F. Halide ions, in particular Cl and F, are well known to play catalytic roles in accelerating aqueous corrosion of iron and steels. The catalytic role has been known to be strongly influenced by the concentration of Cr ions in water.[10] The corrosion acceleration has been attributed to the orders–of–magnitude faster rate of formation of a ligand complex between Fe–halide and H_2O than the rate of formation of a similar complex between halide–free Fe and H_2O. A similar effect can be postulated for reaction rates in forming F–containing (fast) and F–free (slow) ligand complexes of $[FeF(H_2O)_5]^+$ and $[Fe(H_2O)_6]^{2+}$, respectively. A free F ion is then released from the labile complex $FeF(H_2O)_5$ in water when H_2O replaces the F atom in the complex. This cycle can be expressed by:

$Fe\ (lattice) + 6H_2O = [Fe(H_2O)_6]^{2+} + 2e^-$	reaction rate slow	(1)
$Fe–F\ (F\ chemisorbed) + 5H_2O = [FeF(H_2O)_5]^+ + e^-$	rate fast (fast dissolution of Fe)	(2)
$[FeF(H_2O)_5]^+$	labile in water, because	
$[FeF(H_2O)_5]^+ + H_2O = [Fe(H_2O)_6]^{2+} + F^-$	reaction fast, F ion released	(3)

Then, the released F^- ion again drives the fast reaction (2) to form another $[FeF(H_2O)_5]^+$ complex. This cycle repeats itself, leading to a classical catalytic role by F.

However, the reaction chain is broken when the concentration of Cr ions in crack tip water is high, because nonlabile $[CrF(H_2O)_5]^+$ is formed rapidly but remains inert in water. Therefore, F remains trapped in $[CrF(H_2O)_5]^+$ in water, preventing a catalytic role of F.

$Cr\ (lattice) + 6H_2O = [Cr(H_2O)_6]^{2+} + 2e^-$	reaction slow	(4)
$Cr–F\ (F\ adsorbed) + 5H_2O = [CrF(H_2O)_5]^+ + e^-$	rate fast, fast dissolution of Cr	(5)
$[CrF(H_2O)_5]^+$	nonlabile, because	
$[CrF(H_2O)_5]^+ + H_2O = [Cr(H_2O)_6]^{2+} + F^-$	reaction slow	(6)

This traps F atoms in $[CrF(H_2O)_5]^+$ and prevents them from participating in the fast reaction (5), because formation of Cr-F (F chemisorbed on Cr) is minimized.

When O on grain boundaries is high (as in the Type 304L core shroud weld HAZ), Cr and O are bound chemically on the crack tip surfaces. This is in effect equivalent to grain-boundary Cr depletion, because the concentration of Cr ions in crack tip water will be low. Then, F ion concentration in crack tip water will be higher and, as depicted in Fig. 22, the catalytic role of F will be in full force. Thus, susceptibility to "oxyfluorine-assisted" SCC will be influenced strongly by O on grain boundaries in particular, because higher O on grain boundaries is conducive to higher F and more Cr bound to O on the grain boundaries, and hence higher F ion and lower Cr ion concentrations in the crack tip water.

CONCLUSIONS

1. Because of compelling economic advantages, large core internal components such as BWR core shrouds are welded in air by a shielded-metal- or submerged-arc procedure in which welding flux compounds containing CaF_2 are used to produce a plasma shield (weld fume) over the molten metal. Because of exposure to the weld fume, the heat-affected zones of the welds are characterized by significant O and F contamination, whereas contamination in tungsten-inert-gas welds is negligible.

2. Impurity contamination and grain-boundary microstructure of Type 304 and 304L SS BWR core shroud welds and mockup shielded-metal-arc welds were similar. In contrast to those of gas-tungsten-arc welds or laboratory-sensitized base metal, grain boundaries of the heat-affected zones of Type 304 and 304L stainless steel core shroud welds were free of carbide, and neither martensite film nor grain-boundary Cr depletion was observed. Therefore, it is difficult to explain the Type 304 as well as 304L stainless steel core shroud cracking on the basis of either classical intergranular stress corrosion cracking (driven by thermal sensitization) or irradiation-assisted stress corrosion cracking (driven by irradiation-induced grain-boundary Cr depletion).

3. Significant F contamination occurs in association with O contamination, and F content in the heat-affected zone of a core shroud weld is higher in the O-rich region beneath the weld scale, grain boundaries, and oxides. This explains well that weld scale and weld-fume contamination strongly exacerbate the susceptibility of flux welds such as shielded-metal- or submerged-arc welds to intergranular stress corrosion cracking. Evidence indicates that O and F concentrations on grain boundaries of the heat-affected zone of a core shroud weld increase further with long-term operation in reactor. This is expected because solubilities of O and F are negligible in bulk material of the steels and high-energy regions such as grain boundaries are the regions that are favored for segergation of O and F atoms.

4. The failure of the Type 304 and 304L SS core shroud can be explained well by a model based on oxyfluorine-assisted stress corrosion cracking in which a synergism among O, Cr,

and F plays a primary role. According to the model, susceptibility to intergranular stress corrosion cracking is influenced strongly by O and F on grain boundaries. Higher O is conducive to higher F and more Cr bonded to O on the grain boundaries, and hence, higher F ion and lower Cr ion concentrations in the crack-tip water, which allows the strong catalytic role of F.

ACKNOWLEDGMENTS

The authors thank M. B. McNeil and T. F. Kassner for helpful discussions, L. J. Nowicki and W. F. Toter for contributions to the experimental efforts, and T. D. Spry, J. M. Chynoweth, T. Y. Yang, and M. S. Yu for supplying irradiated core-shroud boat samples. This work was supported by the U.S. Nuclear Regulatory Commission, Office of Nuclear Regulatory Research.

REFERENCES

1. J. M. Cookson and G. S. Was, Proc. 7th Intl. Symp. Environmental Degradation of Materials in Nuclear Power Systems - Water Reactors, NACE International, Houston, p. 1109 (1995).
2. H. M. Chung, W. E. Ruther, J. E. Sanecki, A. G. Hins, N. J. Zaluzec, and T. F. Kassner, J. Nucl. Mater., 239 (1996) 61.
3. H. M. Chung, J. H. Park, W. E. Ruther, , J. E. Sanecki, R. V. Strain, and N. J. Zaluzec, Proc. 8th Intl. Symp. on Environmental Degradation of Materials in Nuclear Power Systems - Water Reactors, S. M. Bruemmer, ed., American Nuclear Society, 1997, p. 846.
4. K. Shimizu, K. Kobayashi, G. E. Thompson, P. Skeldon, and G. C. Wood, J. Electrochem. Soc. 144 (1997) 418.
5. C. T. Ward, D. L. Mathis, and R. W. Staehle, Corrosion, 25 (1969) 394.
6. W. E. Berry, E. L. White, and W. K. Boyd, Corrosion 29 (1973) 451.
7. G. J. Theus and J. R. Gels, Corrosion Problems in Energy Conversion and Generation, C. S. Tedmon, Jr., ed., The Electrochemical Society, p. 384 (1974).
8. P. E. C. Bryant and P. R. Habicht, "Fluorine–Induced Intergranular Corrosion of Sensitized Austenitic and Austenoferritic Stainless Steels," Combustion Engineering Internal Report TIS–5065, also in Proc. IAEA Workshop on Stress Corrosion Cracking, March 29-31, 1976.
9. M. Takemoto, T. Shonohara, M. Shirai, and T. Shinogaya, Mater. Perform., 24 (1985) 26.
10. N. C. Huang and Z. Nagy, J. Electrochem. Soc., 134 (1987) 2215.
11. F. Zucchi, G. Trabanelli, and G. Demertzis, Corr. Sci., 28 (1988) 69.
12. P. L. Andresen, Proc. EPRI Workshop on Significance and Control of Chromate in BWRs, Nov. 13–14, 1990, Chicago.
13. C. K. Lee and H. C. Shih, Corrosion, 52 (1996) 690.

TABLE 1
COMPOSITION (IN WT.%) OF TYPE 304, 304L, AND 316 STAINLESS STEELS

ANL Heat ID	Steel Type	Thickness (mm)	Weld Type Investigated	Ni	Si	P	S	Mn	C	N	Cr	Mo
C1	304	12.7	SMA, GTA	8.12	0.50	0.038	0.002	1.00	0.060	0.060	18.11	–
C3	304L	12.7	SMA, GTA	8.91	0.46	0.019	0.004	1.81	0.016	0.083	18.55	–
C21	316	12.7	SMA, GTA	10.24	0.51	0.034	0.001	1.19	0.060	0.020	16.28	2.08
19611	304	38	SMA	8.36	0.48	0.024	0.018	1.69	0.060	0.086	18.35	0.14
M9284	304	38	SMA, GTA	8.12	0.45	0.021	0.011	1.47	0.050	0.055	18.49	0.28

TABLE 2
COMPOSITION (IN WT.%) AND FLUENCE OF CRACKED BWR CORE SHROUD WELDS

ANL ID of Specimen	Source BWR	Steel Type	Cracked Weld Boat Sample	Composition (wt.%) Cr	Ni	Mn	C	Nb	Mo	Si	P	S	Fluence (10^{19} n·cm^{-2})
507-B[a]	BWR-C	304L	H3, ID	18.90	9.36	1.82	0.027	0.064	0.568	0.483	0.024	0.0018	4.6
D3-H5-324	BWR-D	304	H5, OD	-	-	-	0.063[b]	-	-	-	-	-	10
QC-1	BWR-Q	304	H5, OD	-	-	-	0.063[b]	-	-	-	-	-	0.003

[a]Composition determined for irradiated boat sample by electron probe microanalysis.
[b]Carbon content of unirradiated plate.

TABLE 3
COMPOSITION (IN WT.%) OF E-308-16 WELDING ELECTRODE

Fe	Cr	Ni	Mn	Si	Mo	C	Cu	Nb	V	F	$CaCO_3$	CaF_2	SiO_2	TiO_2	Al_2O_3	Silicate
67.5	20.3	9.7	1.17	0.52	0.39	0.052	0.1	0.02	0.07	2.86	2-8	1-10	1-8	1-12	0-3	<5

TABLE 4
COMPOSITION OF BASE METAL AND SMA AND GTA WELD HAZS, TYPE 304 SS HEAT C1

	SMA-HAZ	GTA-HAZ	Base Metal
	wt.%		
Cr	19.91	18.88	18.11
Ni	9.36	9.60	8.12
Mn	1.18	1.30	1.00
Mo	0.27	0.06	<0.05
Cu	0.07	0.05	0.05
Si	0.56	0.47	0.50
	wppm		
C	600	600	600
O	640	97	80
P	310	330	380
S	50	20	20
	appm		
F	20-240	negligible	negligible

TABLE 5
SUMMARY OF TEM CHARACTERIZATION OF THERMAL SENSITIZATION IN HEAT-AFFECTED ZONES OF MOCKUP SMA AND GTA WELDS

Steel Type	ANL Heat ID	Fluence (E > 1 MeV) (n cm^{-2})	Base Metal Carbon (wt.%)	Base Plate Thickness (mm)	Weld Type	GB Carbides Detected by TEM	Carbides Detected by SIMS
304	C1	0	0.060	12.7	SMA	**none**	**none**
304	C1	0	0.060	12.7	GTA	many	many
304L	C3	0	0.016	12.7	SMA	**none**	**none**
304L	C3	0	0.016	12.7	GTA	none	–
316	C21	0	0.060	12.7	SMA	**none**	–
316	C21	0	0.060	12.7	GTA	some	–
304	19611	0	0.060	38	SMA	**none**	–
304	M9284	0	0.050	38	SMA	**none**	–
304	M9284	0	0.050	38	GTA	many	–
304L core shroud	BWR-C	4.6×10^{19}	0.027	38	SMA	**none**	–
304 core shroud	BWR-D	10×10^{19}	0.063	50.8	SMA	**none**	–

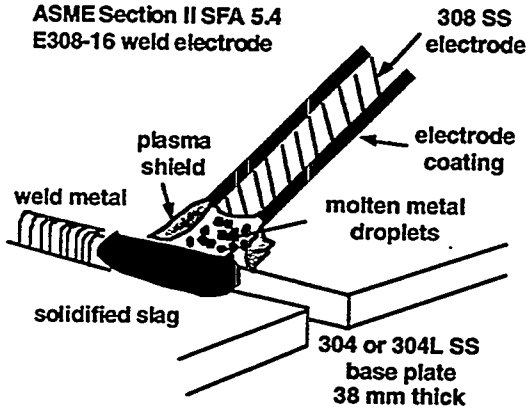

FIGURE 1:
Schematic illustration of shielded-metal-arc welding procedure.

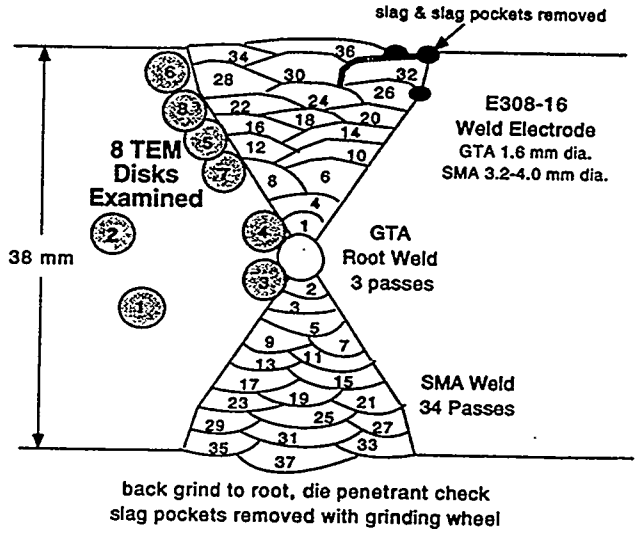

FIGURE 2:
Schematic diagram of weld passes and TEM disk locations of a 38-mm-thick plate of Type 304 SS, Heat 19611. Weld slag and slag pockets were removed after each pass.

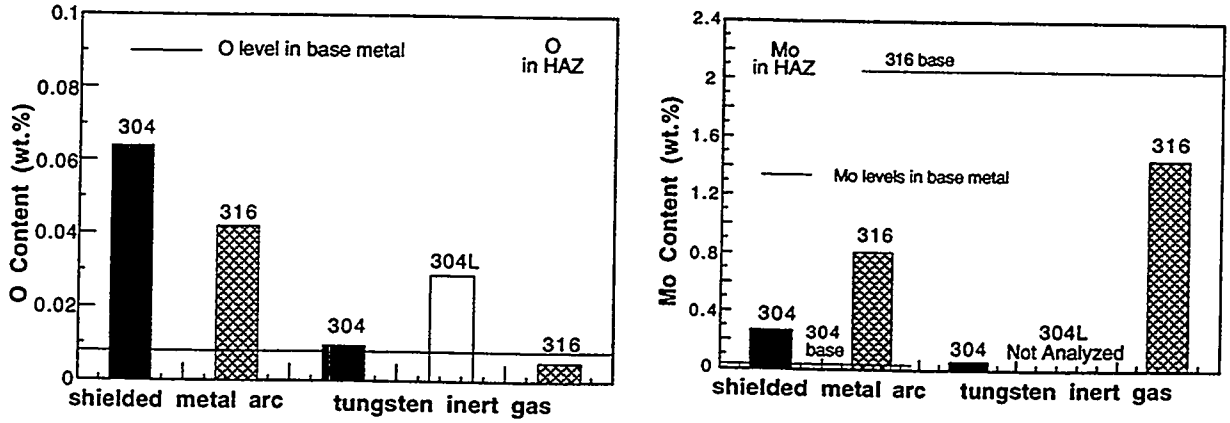

FIGURE 3: Oxygen (left) and Mo (right) contents of SMA and GTA weld HAZs.

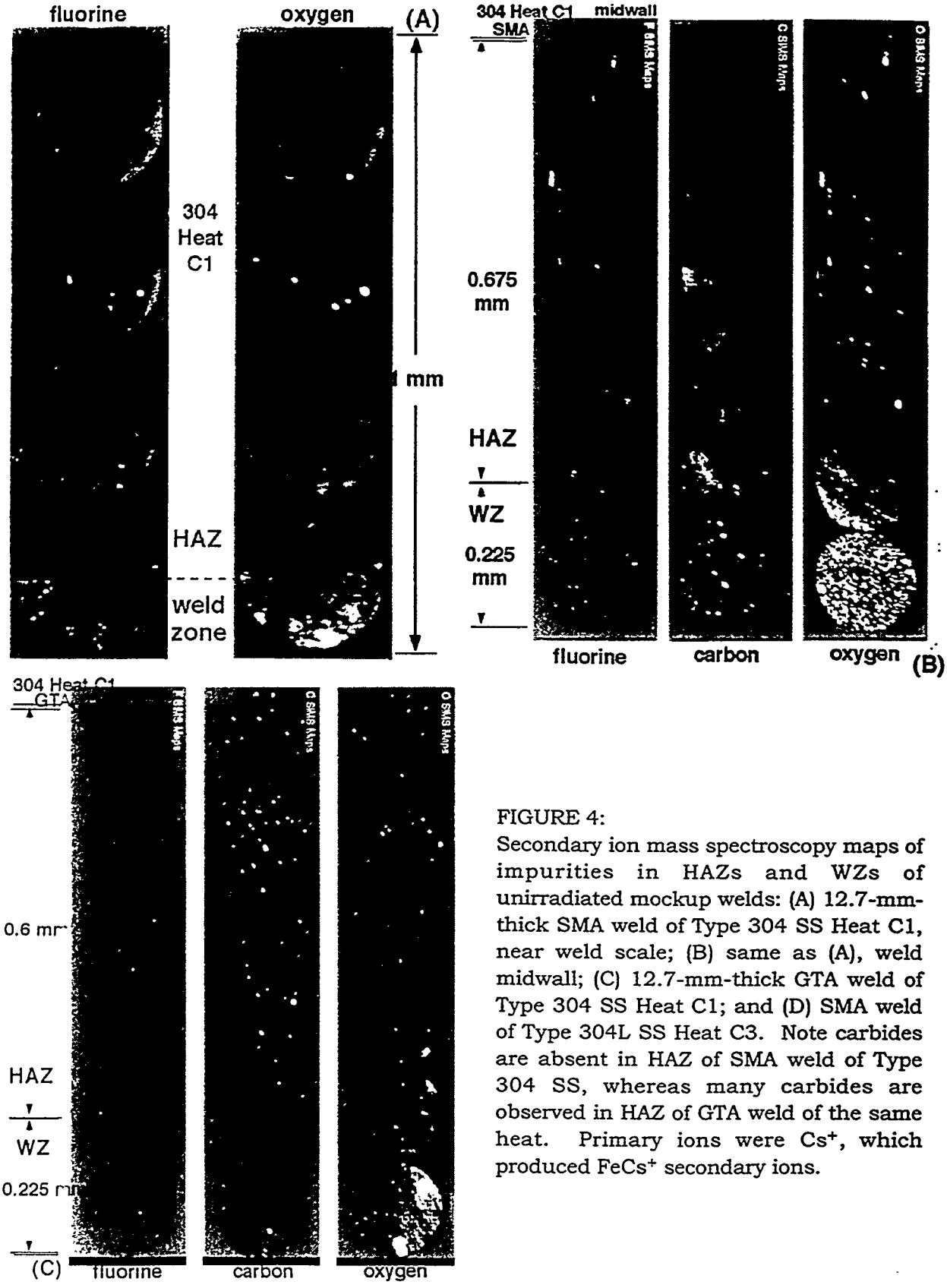

FIGURE 4:
Secondary ion mass spectroscopy maps of impurities in HAZs and WZs of unirradiated mockup welds: (A) 12.7-mm-thick SMA weld of Type 304 SS Heat C1, near weld scale; (B) same as (A), weld midwall; (C) 12.7-mm-thick GTA weld of Type 304 SS Heat C1; and (D) SMA weld of Type 304L SS Heat C3. Note carbides are absent in HAZ of SMA weld of Type 304 SS, whereas many carbides are observed in HAZ of GTA weld of the same heat. Primary ions were Cs^+, which produced $FeCs^+$ secondary ions.

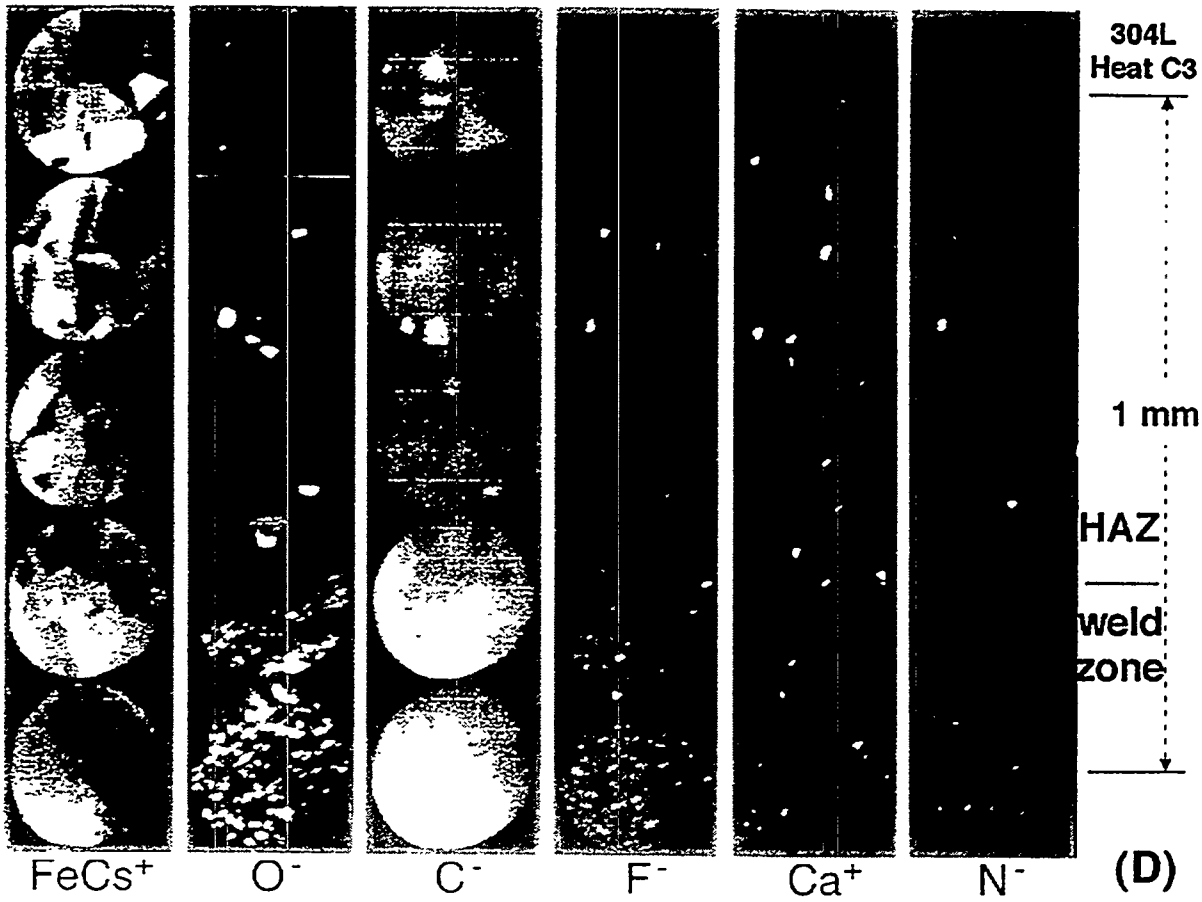

FIGURE 4: Continued.

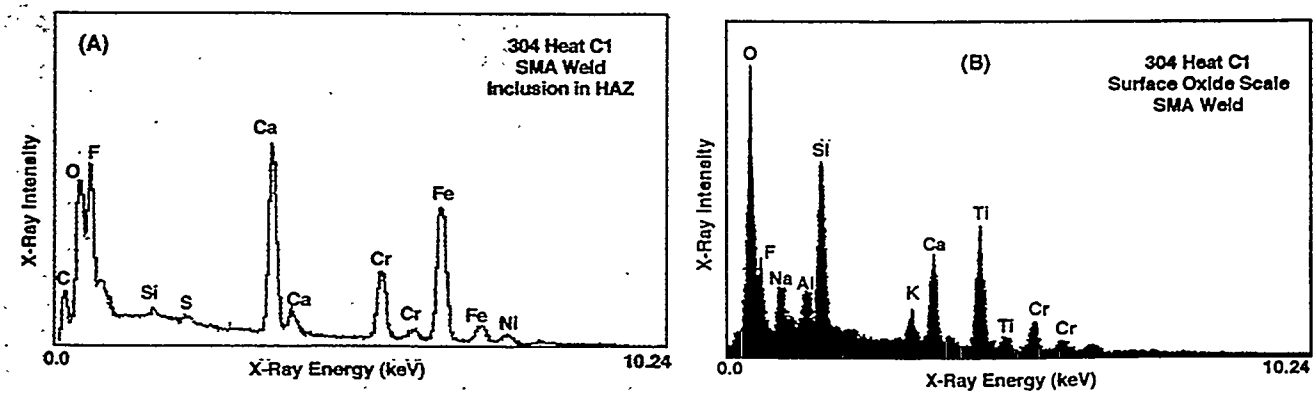

FIGURE 5: Composition of (left) Ca-rich precipitates in HAZ and (right) surface weld scale of unirradiated SMA weld of Type 304 SS Heat C1 that were analyzed by X-ray energy-dispersive spectroscopy in SEM.

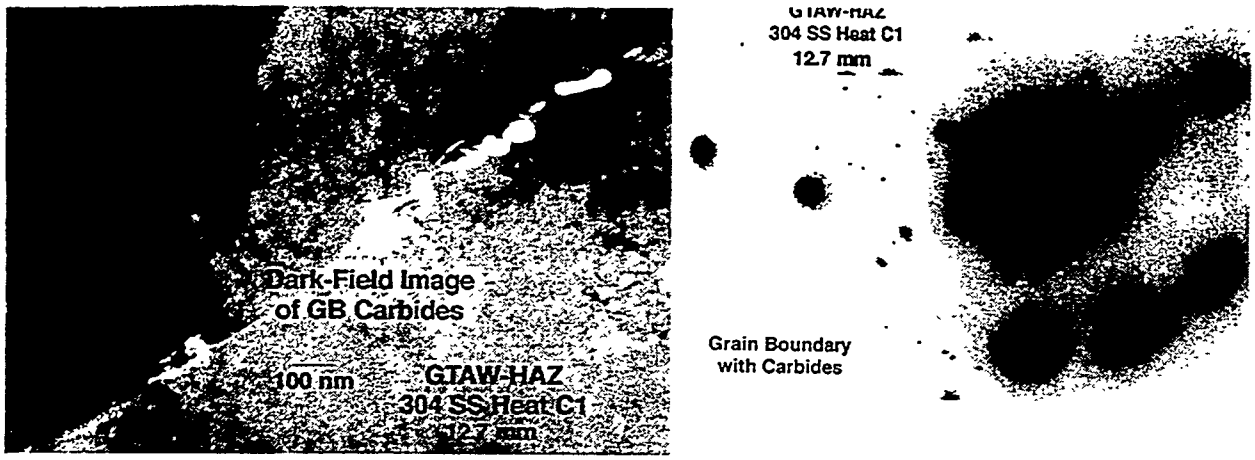

FIGURE 6: Dark-field image (left) and characteristic selected-area diffraction pattern (right) of $M_{23}C_6$ carbides from a grain boundary of heat-affected zone of nonirradiated GTA weld of Type 304 SS, Heat C1, showing significant thermal sensitization.

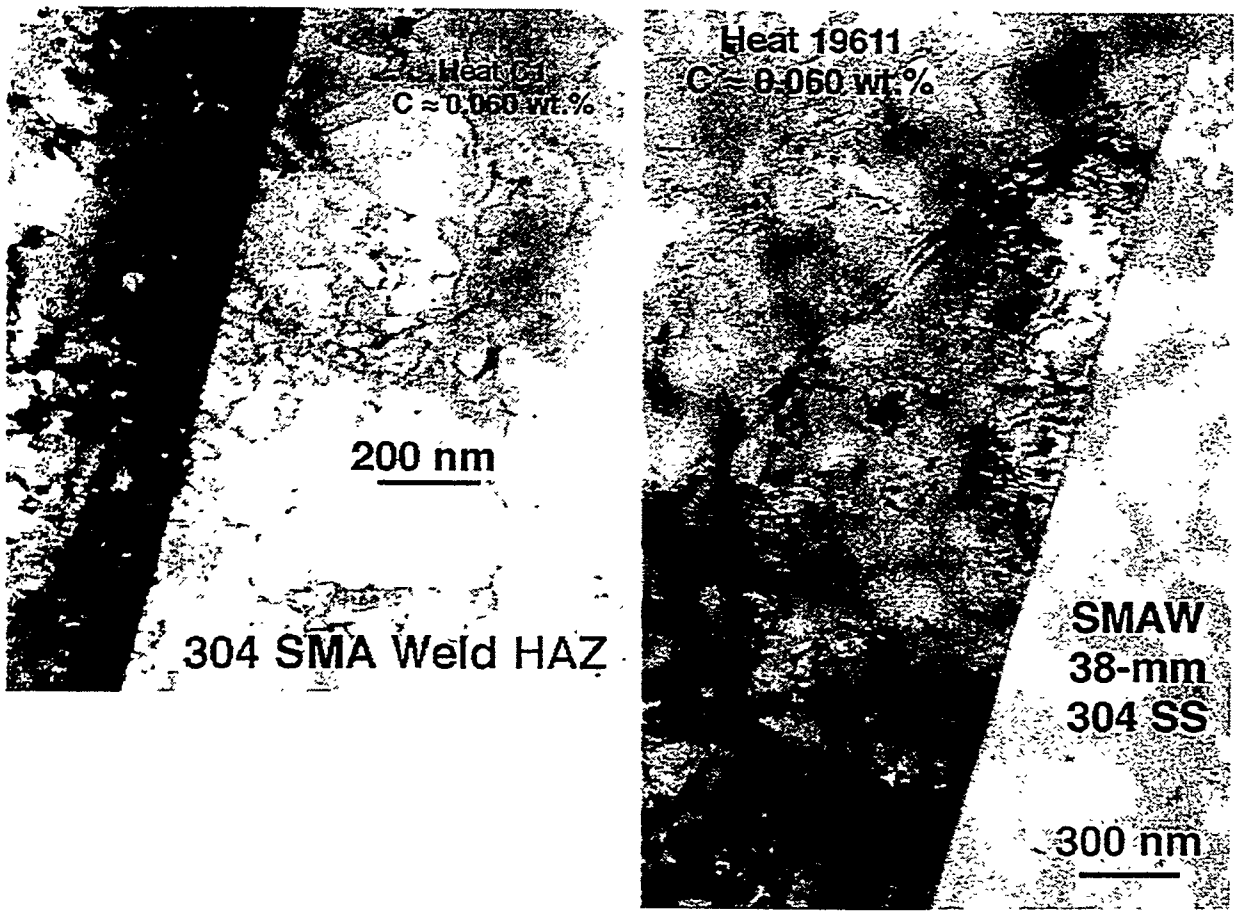

FIGURE 7: Bright-field images of grain boundaries of HAZs of nonirradiated SMA welds of Type 304 SS, Heat C1 (left, 12.7-mm-thick plate, ≈0.060 wt.% C) and Heat 19611 (right, 38-mm-thick plate, ≈0.060 wt.% C). Note absence of carbides.

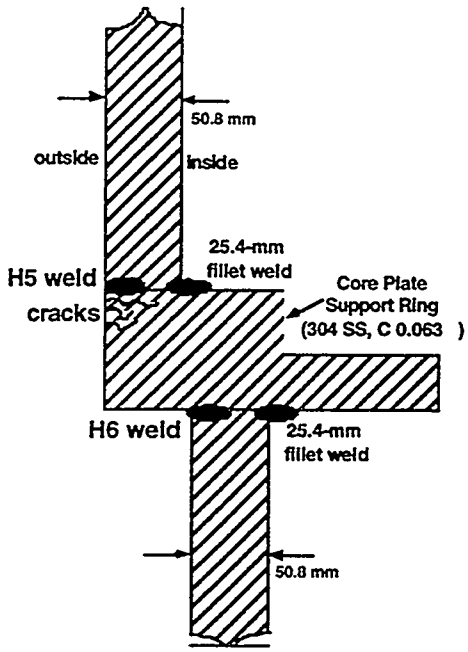

FIGURE 8:
Schematic diagram of H5 and H6 welds and cracked core plate support ring of BWR-D.

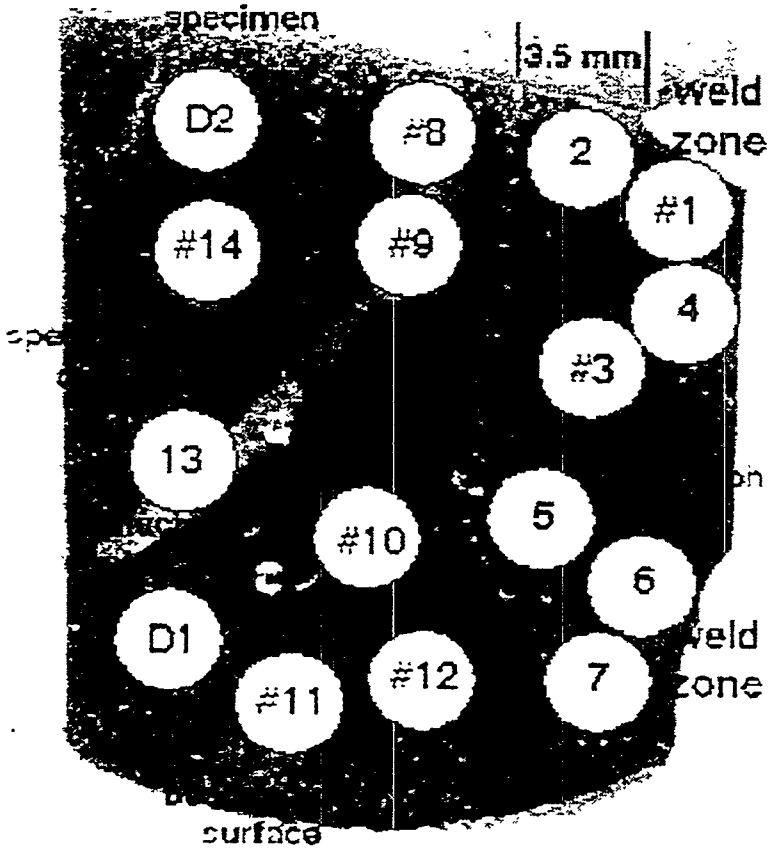

TEM Disk Location, BWR-D H5 Weld Crack

FIGURE 9:
Location of cracks and TEM disks in boat sample from a Type 304 SS core shroud weld from BWR-D irradiated to a fluence of ≈1 x 10^{20} n·cm^{-2} (E >1 MeV). Disks 1, 3, 8, 9, 10, 11, 12, and 14 were examined. No grain-boundary carbides were observed in any of the disks.

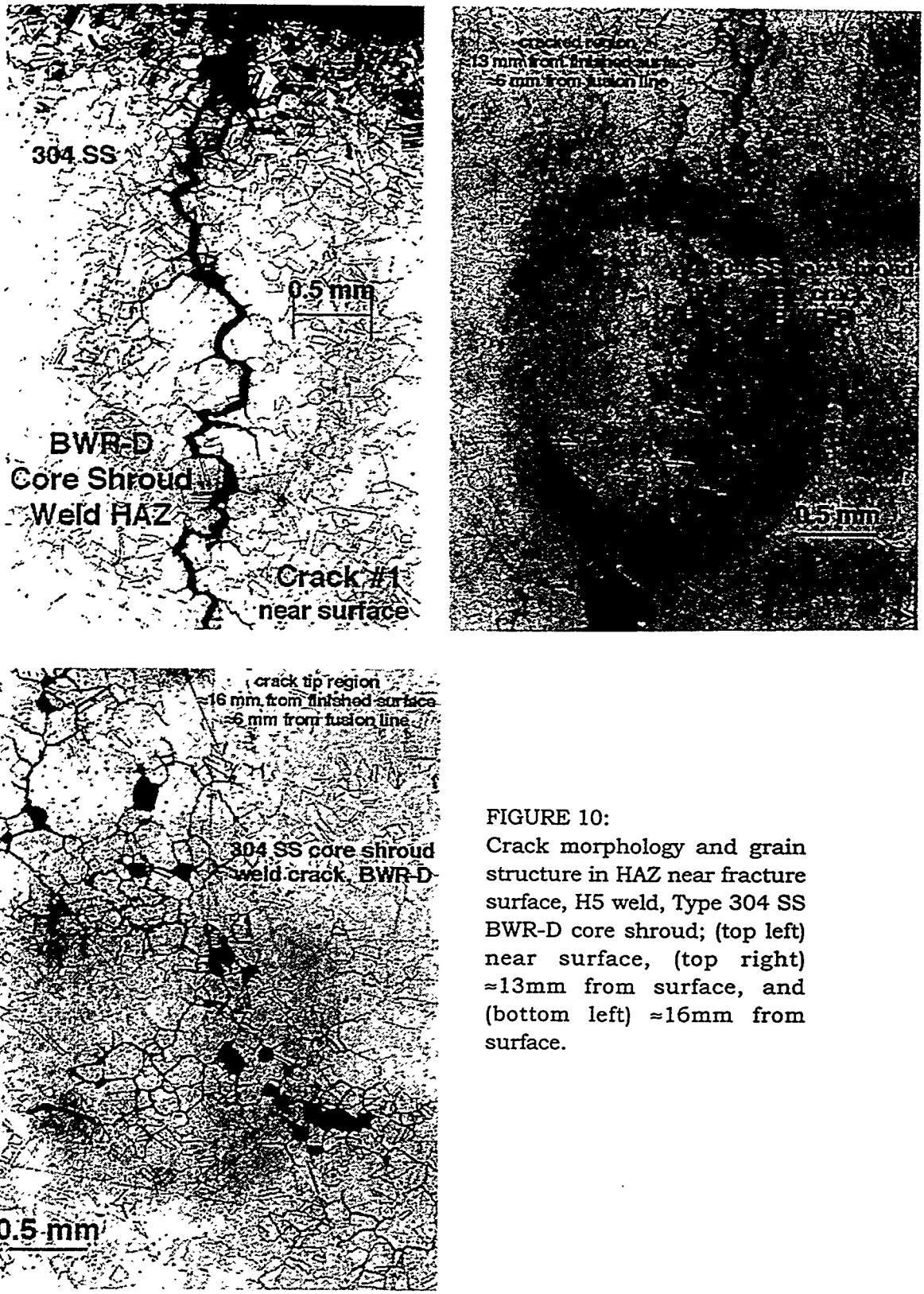

FIGURE 10:
Crack morphology and grain structure in HAZ near fracture surface, H5 weld, Type 304 SS BWR-D core shroud; (top left) near surface, (top right) ≈13mm from surface, and (bottom left) ≈16mm from surface.

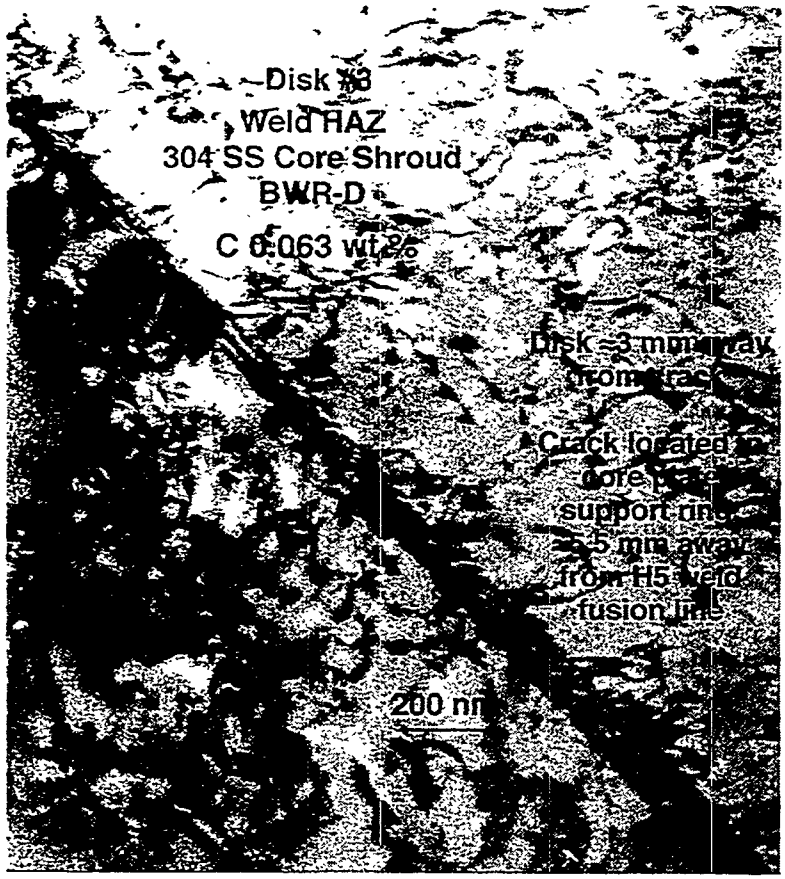

FIGURE 11:
Typical example of grain boundaries in HAZ of Type 304 SS cracked core shroud weld irradiated to a fluence of ≈1 x 10^{20} n·cm^{-2} (E >1 MeV) in BWR-D. Note thickness fringes and absence of carbides on grain boundaries.

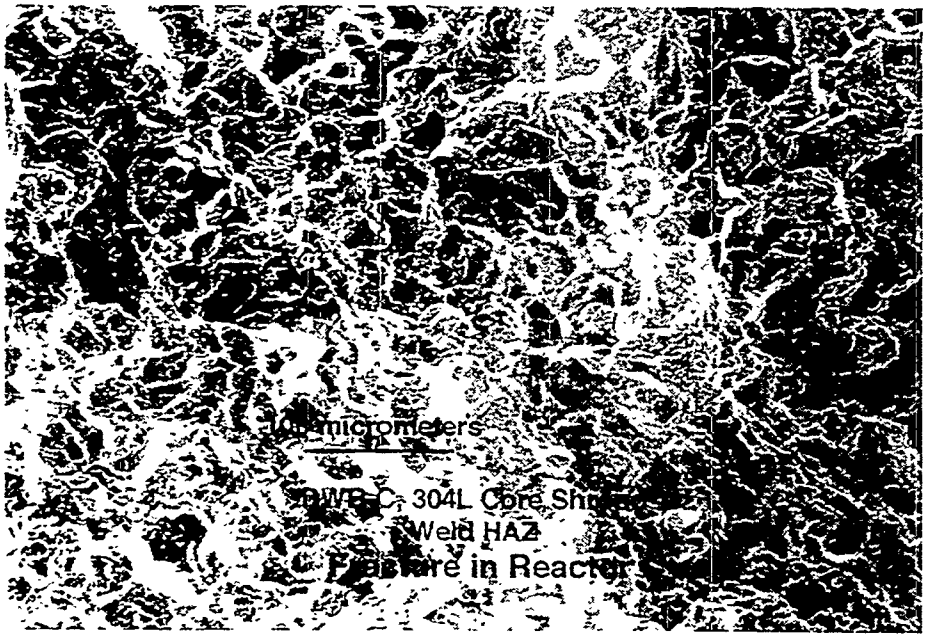

FIGURE 12:
SEM fracture surface morphology of Type 304L BWR-C core shroud weld. Fracture occurred in HAZ during service, fluence 0.45 x 10^{21} n·cm^{-2} (E > 1 MeV).

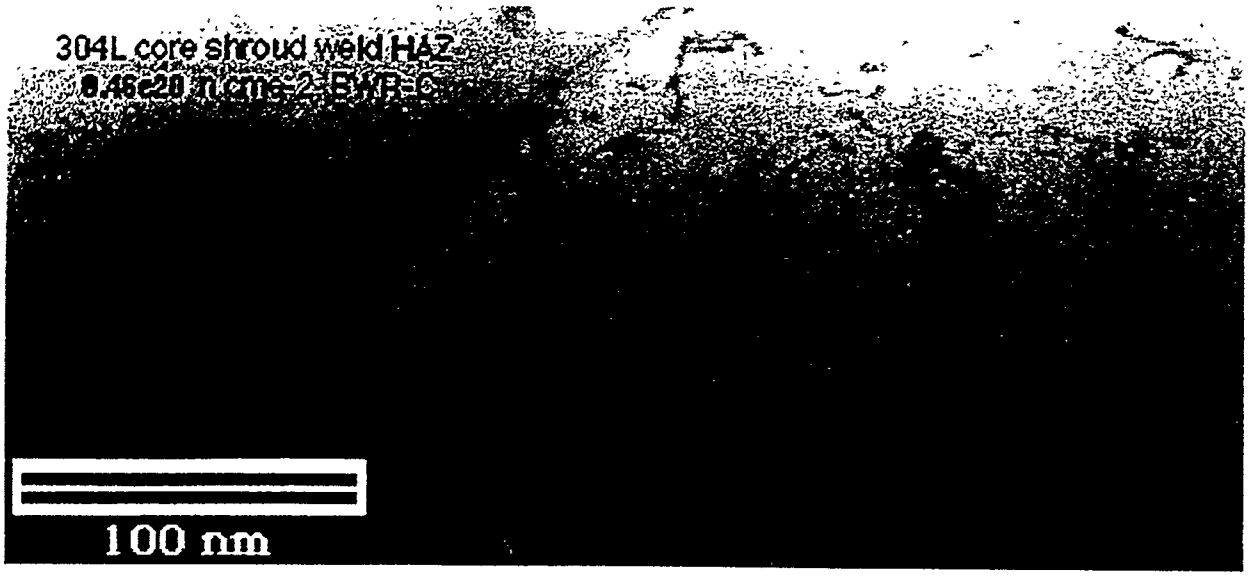

FIGURE 13:
Typical grain-boundary structure of HAZ of Type 304L BWR-C core shroud weld. Carbides and thin films are absent from the boundary.

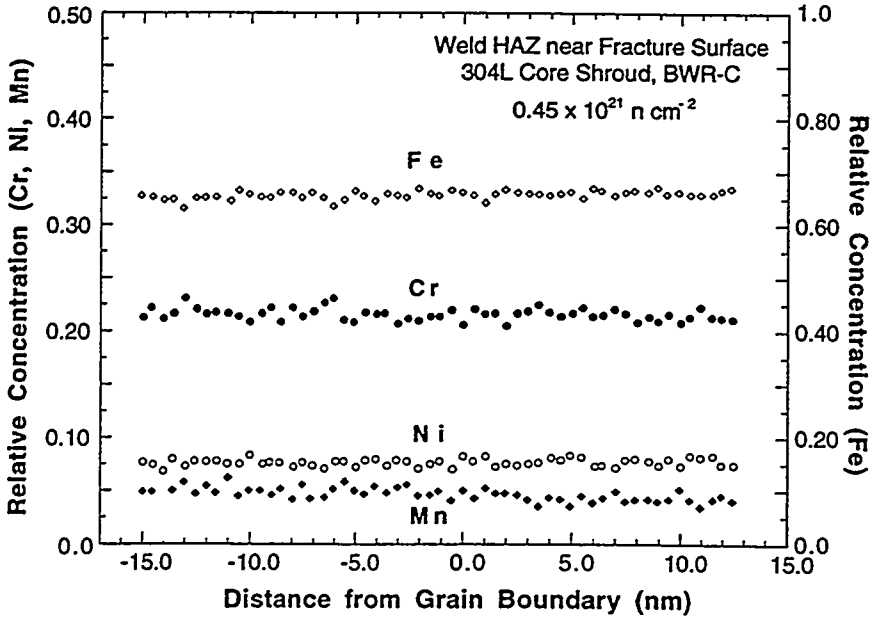

FIGURE 14:
Profiles of Fe, Cr, Ni, and Mn near grain boundary of Type 304L BWR-C core shroud weld HAZ shown in Fig. 9. Grain-boundary Cr depletion is negligible.

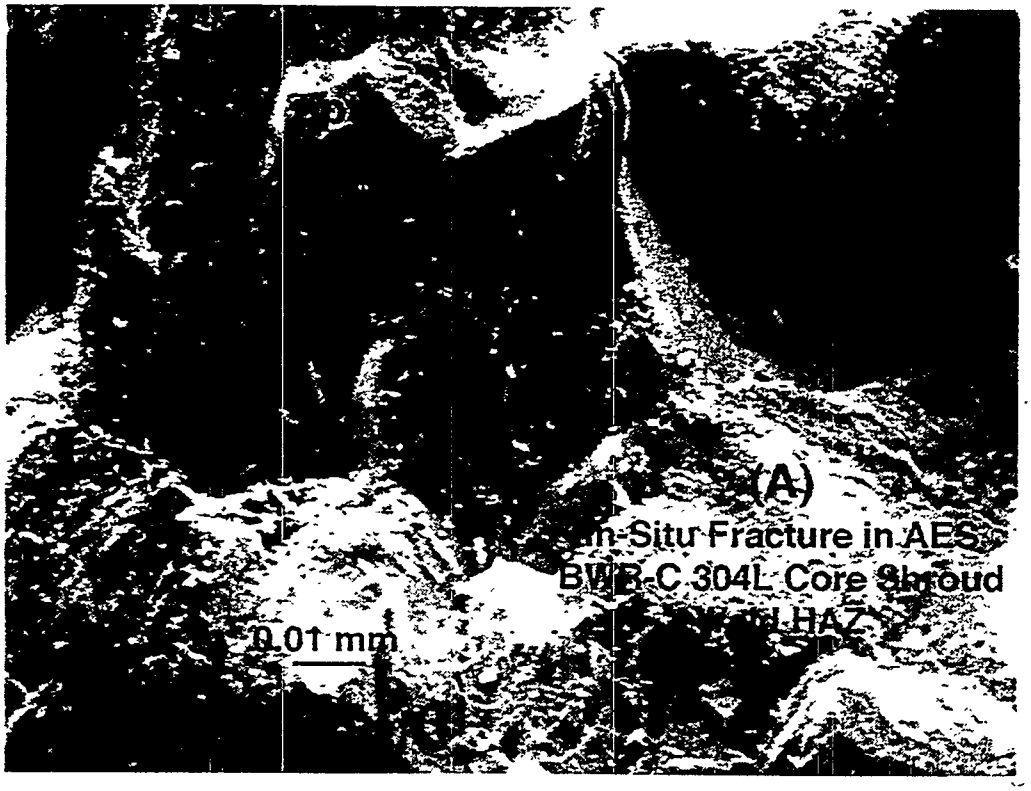

FIGURE 15:
AES in-situ fracture surface morphology in HAZ of Type 304L BWR-C core shroud weld, in which fracture was produced at ≈23°C in ultrahigh vacuum of scanning Auger electron microscope. Many fine oxide particles are present on the fracture surface.

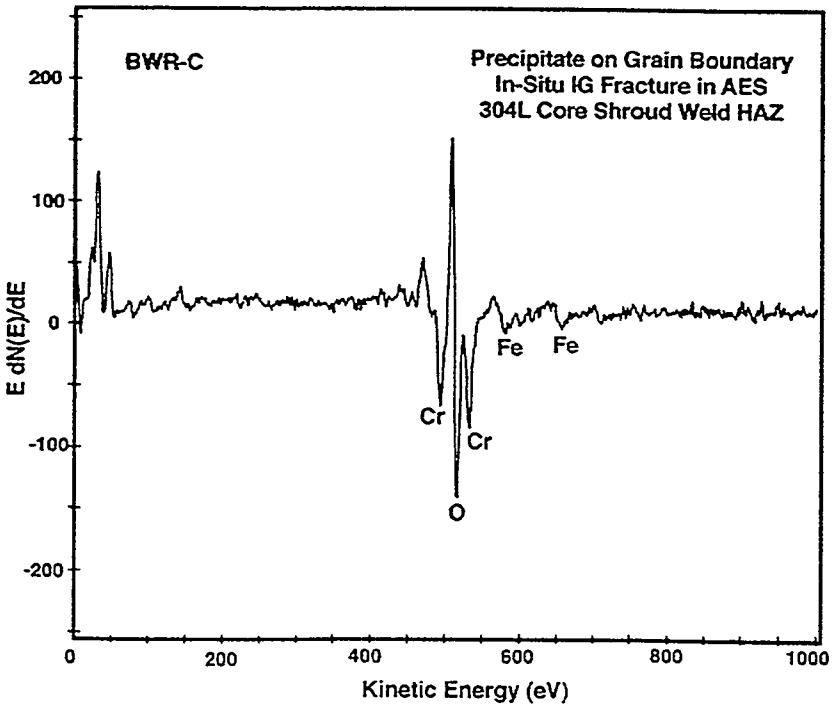

FIGURE 16:
AES signals from particle denoted "ppt" in Fig. 15, showing composition of a chromium oxide.

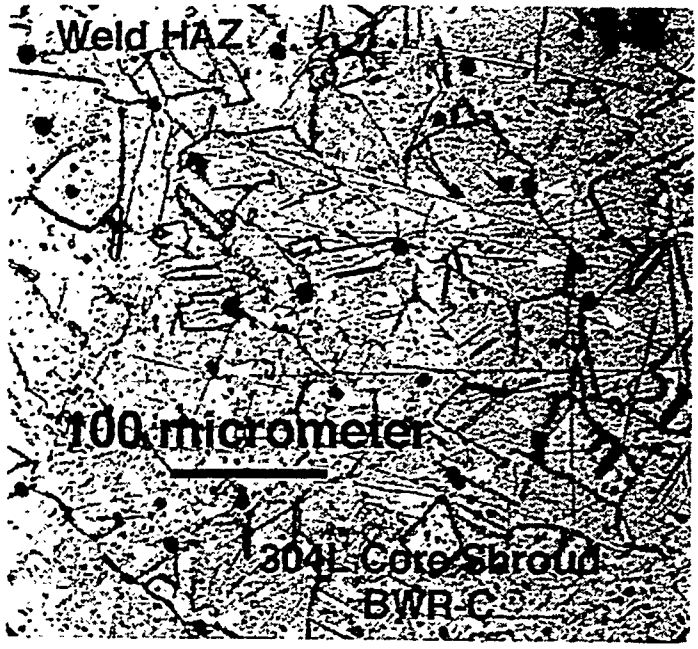

FIGURE 17:

Optical photomicrograph of HAZ near fracture surface of cracked H3 weld in BWR-C core shroud, Type 304L SS. White arrows denote inclusions located near or on grain boundaries.

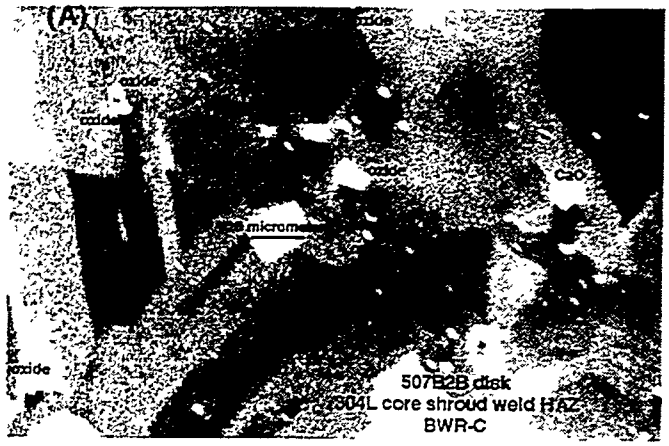

FIGURE 18:

AES secondary-electron image of polished and Ar-ion-sputter region of HAZ near fracture surface, H3 weld, Type 304L SS BWR-C core shroud (A). Each precipitate denoted as "oxide" or "CaO" was identified by analyzing AES spectra from the precipitate. Spectra from Fe oxide and CaO are shown in (B) and (C), respectively.

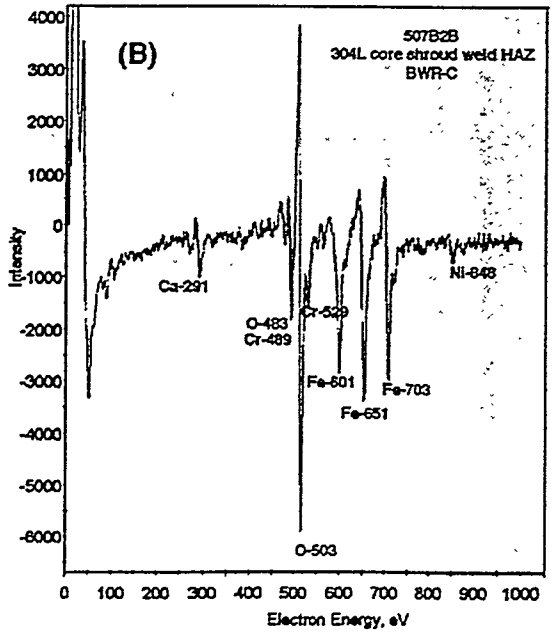

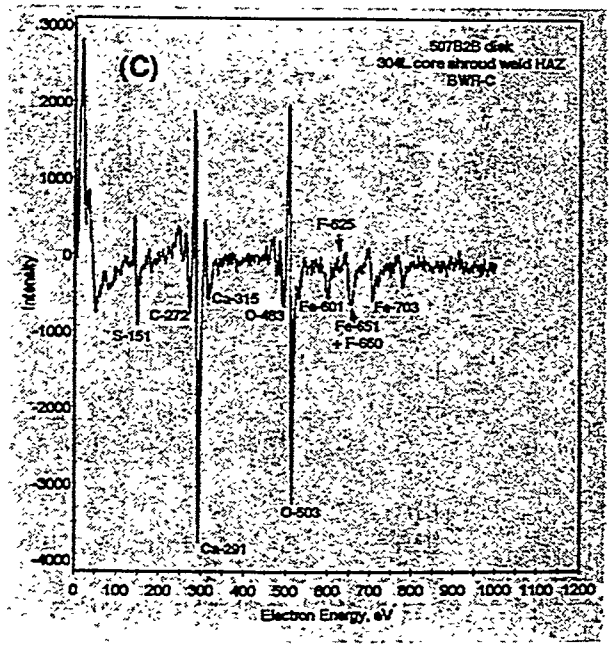

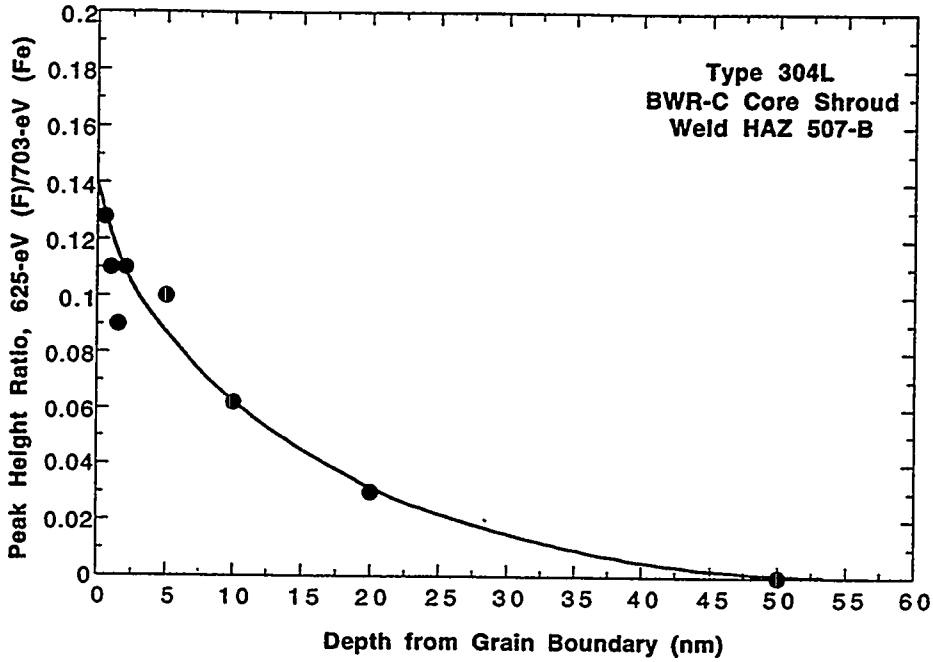

FIGURE 19:
Fluorine AES signal intensity as function of sputter distance from grain boundary surface in HAZ of Type 304L BWR-C core shroud weld

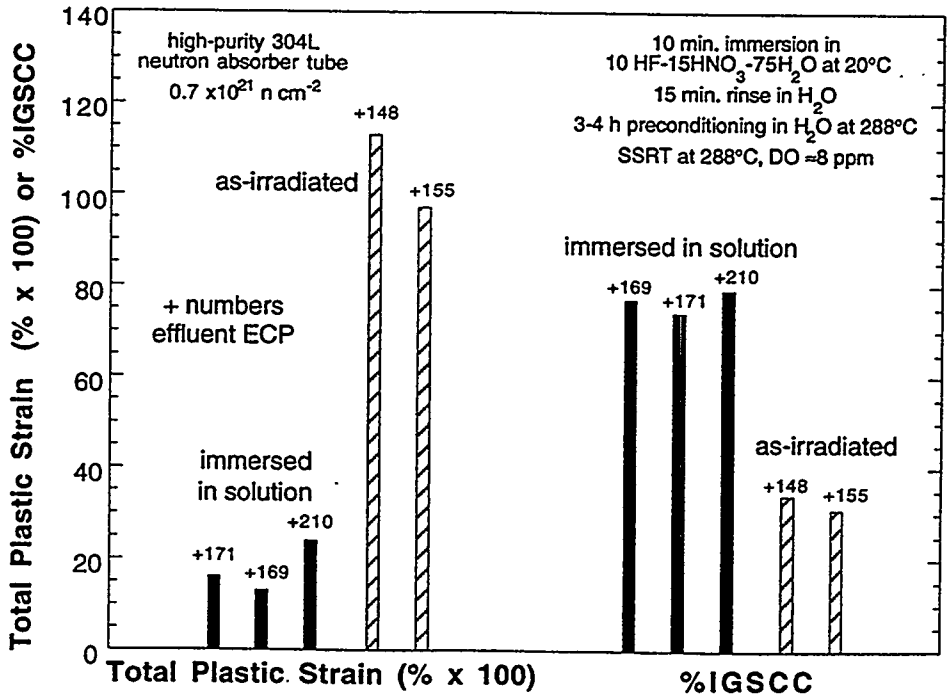

FIGURE 20:
Effect of F contamination by immersion in HF-containing solution on total plastic strain and percent IGSCC; high-purity Type 304L neutron absorber tube, fluence (E> 1 MeV) 0.7 x 10^{21} n·cm^{-2}.

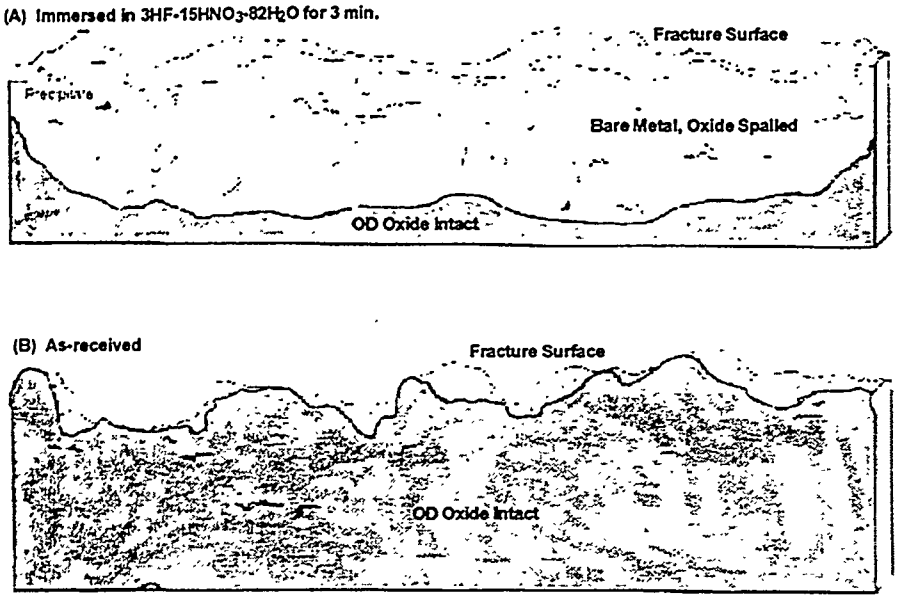

FIGURE 21:
"Sloughed-off" oxide and dense crack on OD surface of Type 304 SS neutron-absorber tubes (fluence 2.0 x 10^{21} n·cm^{-2}) tested after fluorine contamination in 3HF–15HNO$_3$–82H$_2$O solution for 3 min (top) and in as-irradiated state (bottom).

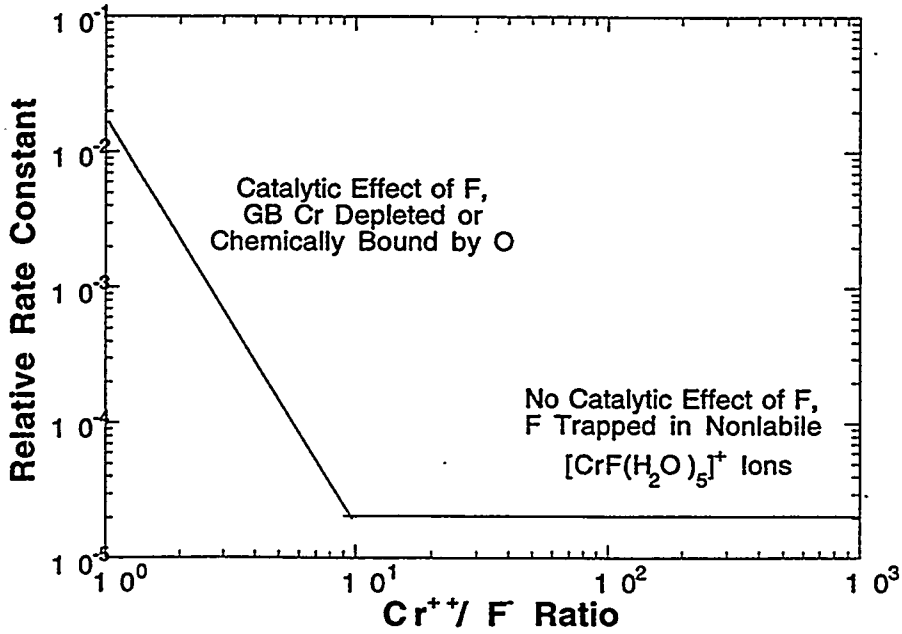

FIGURE 22:
Schematic illustration of effects of O and F on grain boundaries and Cr ion in crack-tip water on oxyfluorine-assisted SCC